Vesicle shrinkage in hydrous phonolitic melt during cooling

A. Allabar[1] · K. J. Dobson[2,3] · C. C. Bauer[4] · M. Nowak[1]

Abstract

The ascent of hydrous magma prior to volcanic eruptions is largely driven by the formation of H_2O vesicles and their subsequent growth upon further decompression. Porosity controls buoyancy as well as vesicle coalescence and percolation, and is important when identifying the differences between equilibrium or disequilibrium degassing from textural analysis of eruptive products. Decompression experiments are routinely used to simulate magma ascent. Samples exposed to high temperature (T) and pressure (P) are decompressed and rapidly cooled to ambient T for analysis. During cooling, fluid vesicles may shrink due to decrease of the molar volume of H_2O and by resorption of H_2O back into the melt driven by solubility increase with decreasing T at $P < 300$ MPa. Here, we quantify the extent to which vesicles shrink during cooling, using a series of decompression experiments with hydrous phonolitic melt (5.3–3.3 wt% H_2O, T between 1323 and 1373 K, decompressed from 200 to 110–20 MPa). Most samples degassed at near-equilibrium conditions during decompression. However, the porosities of quenched samples are significantly lower than expected equilibrium porosities prior to cooling. At a cooling rate of 44 K·s^{-1}, the fictive temperature T_f, where vesicle shrinkage stops, is up to 200 K above the glass transition temperature (T_g), Furthermore, decreasing cooling rate enhances vesicles shrinkage. We assess the implications of these findings on previous experimental degassing studies using phonolitic melt, and highlight the importance of correctly interpreting experimental porosity data, before any comparison to natural volcanic ejecta can be attempted.

Keywords Decompression experiments · Vesiculation · Vesicle shrinkage · Quench effect · H_2O resorption · Fictive temperature

✉ A. Allabar
anja.allabar@uni-tuebingen.de

1   Department of Geosciences, University of Tübingen, Wilhelmstraße 56, 72074 Tübingen, Germany

2   Department of Earth Sciences, Durham University, Durham DH1 3LE, UK

3   Civil & Environmental Engineering, University of Strathclyde, Glasgow G1 1XJ, UK

4   Department of Geosciences, University of Tübingen, Hölderlinstr. 12, 72074 Tübingen, Germany

Introduction

Volcanic eruptions are driven by magma density decrease caused by the exsolution of volatiles, mainly H_2O (e.g., Gonnermann and Manga 2007). H_2O supersaturation of the melt can be induced by a pressure (P) decrease and causes formation of vesicles, which then grow by both pressure related equation of state (EOS) expansion and continuous diffusion of H_2O from the melt into the fluid phase (e.g., Sparks 1978). The porosity of a magma is a key parameter influencing the buoyancy and thus driving the acceleration of magma during ascent.

In experimental studies, the porosity of decompressed silicate melts subsequently quenched to glass has been used to investigate vesicle growth and coalescence as well as the evolution of permeability or percolation (Giachetti et al. 2019; Lindoo et al. 2016). Porosity has also been used to distinguish between equilibrium or disequilibrium degassing by comparing the glass porosity (Φ_{glass}) or the residual H_2O concentration in the glass ($c_{H2Oglass}$) with

those at experimental equilibrium conditions (e.g., Gardner 2012; Larsen and Gardner 2004; Mangan and Sisson 2000; Iacono-Marziano et al. 2007).

However, vesicles may shrink during cooling through a decrease in molar volume of H_2O fluid (V_{mH2O}) within the vesicles (EOS shrinkage; Marxer et al. 2015), and because of the increasing isobaric solubility of H_2O in silicate melt with decreasing T at $P < 300$ MPa (Holtz et al. 1995; Schmidt and Behrens 2008), leading to resorption of H_2O from the fluid vesicles back into the melt (McIntosh et al. 2014; Ryan et al. 2015). Together, these processes lead to a reduction in porosity, and increase the H_2O concentration (c_{H2O}) of the melt during cooling before the supercooled melt is quenched to a glass. Measured Φ_{glass} and $c_{H2Oglass}$ therefore may not represent the molten state of the sample prior to cooling, especially when cooling rates are low. Slow cooling (~ 10 K·min^{-1}) in sintering experiments using rhyolitic glass powder (T of 1023–823 K, P of 22 MPa and H_2O concentrations up to ~ 2.2 wt%) in the presence of fluid leads to resorption of H_2O vesicles resulting in fully dense obsidian (Gardner et al. 2019).

Cooling rates in decompression experiments are usually much faster (up to 150 K s^{-1}), but T and c_{H2O} are significantly higher and melt viscosities are lower compared to the sintering experiments of Gardner et al. (2019). Consequently, vesicle shrinkage is still expected during cooling of vesiculated melts (McIntosh et al. 2014; Marxer et al. 2015; Allabar and Nowak 2018). McIntosh et al. (2014) have found that during fast cooling of experimentally decompressed phonolitic melt to ambient T within 3–10 s significant resorption occurs, demonstrating that the state prior to quench cannot be frozen in. Therefore, we further investigate this effect and quantify vesicle shrinkage and H_2O resorption during cooling on an existing data set of vesiculated phonolitic melt with white pumice composition of the AD79 Vesuvius eruption (VAD79; Iacono-Marziano et al. 2007) quenched to glass. By applying different cooling rates (q) on these vesiculated phonolitic melts by additional experiments, we determine the influence of q on the extent of vesicle shrinkage.

Calculations were performed to quantify the effect of shrinkage during cooling, driven by the EOS of the H_2O fluid and resorption of H_2O back into the melt. To determine the fictive temperature (T_f) where vesicle shrinkage stops, Φ_{glass} was used as well as the liquid water to vesicle volume ratio at ambient conditions derived from X-ray computed tomography (XCT) data. Finally, the results of this study are compared to previous decompression experiments with hydrous phonolitic melt and discussed with respect to the possible effect of vesicle shrinkage. Variables used in this publication are listed in Table 1.

Experimental and analytical methods

Decompression experiments

We augment a series of decompression experiments from Allabar and Nowak (2018) and Allabar et al. (2020) (Table 2) to quantify vesicle shrinkage during cooling of vesiculated VAD79 phonolitic melts. The experiments of these studies were conducted in an internally heated argon pressure vessel (IHPV) at decompression temperatures (T_d) of 1323–1373 K and initial dissolved H_2O contents (c_{H2Oini}) of 5.3, 4.3, and 3.3 wt%. Decompression rates were 0.064–1.7 MPa·s^{-1}, starting from initial P of 200 MPa to final P (P_{final}) ranging between 110–20 MPa. At P_{final}, samples were cooled with a medium quench rate (MQ, although reported as RQ in Allabar and Nowak 2018). Samples were quenched by melting a platinum wire, at which the sample capsules were fixed during the experiments, leading to a capsule drop into the cold zone of the samples holder (Berndt et al. 2002) that was equipped with a brass rod at the bottom to reduce cooling rate (see "quantification of cooling rate"). This procedure was necessary to obtain intact samples for analysis.

The experiments of this study were performed on the same starting material and at identical run temperature as in Allabar and Nowak (2018) and Allabar et al. (2020), with c_{H2Oini} of 5.3 wt% and a decompression rate of 0.17 MPa s^{-1}. However, different quench protocols were applied, to investigate the influence on the Φ_{glass} of the finally analyzed glassy samples. Synthetic VAD79 glass cylinders with 5 mm diameter and 6.5 mm length were inserted together with 5.3 wt% H_2O into Au80Pd20 tubes (13 mm length, 5 mm inner diameter) that were welded shut with a lid at the bottom. After sample filling, the upper ends of the capsules were crimped to a three sided star and welded. Possible leakage was checked by storing the capsules in a compartment dryer at 383 K, pressurizing to 100 MPa at ambient T, and again storing at 383 K. The capsules were re-weighed after each step. Constant capsule weight ruled out leakage and qualified the capsules for the experiments.

The samples were hydrated in the IHPV at slightly H_2O undersaturated conditions at 200 MPa and superliquidus T of 1523 K for at least 94 h to obtain a homogeneous hydrous melt. After hydration, T was decreased to the decompression temperature T_d of 1323 K, still above the liquidus (Iacono-Marziano et al. 2007; Marxer et al. 2015; Allabar et al. 2020). The thermal gradient, measured by two thermocouples close to the samples over a distance of ~ 12 mm, is < 20 K. The T gradient within the samples is assumed to be < 10 K because the sample length of 6.5 mm is lower than the distance between the two thermocouples. The samples were equilibrated at T_d for at least 0.5 h before

Table 1 Symbol definitions

Symbol	Definition	Unit
B_s	Vesicle shrinkage factor	
c_{H2O}	H_2O concentration	wt%
c_{H2Oequ}	Equilibrium H_2O concentration	wt%
$c_{H2Oglass}$	H_2O concentration in glass after quench	wt%
c_{H2Oini}	Initial H_2O concentration in the melt prior to decompression	wt%
c_{H2OIR}	H_2O concentration in the glass measured with FTIR close to vesicles	wt%
c_{H2Ores}	Maximum possible resorbed c_{H2O} assuming resorption to T_g	wt%
c_{H2Ores_Tf}	Residual c_{H2O} at T_f	wt%
D_{H2O}	Diffusivity of H_2O in silicate melt	$mm^2 \cdot s^{-1}$
dP/dt	Decompression rate	$MPa \cdot s^{-1}$
l	Characteristic diffusion length	mm
P	Pressure	MPa
P_{final}	Final pressure where samples were quenched	MPa
q	Quench rate; NQ = 16 K s^{-1}; MQ = 44 K s^{-1}	$K \cdot s^{-1}$
r	Radius	m
T	Temperature	K
T_d	Run temperature of decompression experiment	K
T_f	Fictive temperature where vesicle shrinkage effectively stops	K
T_g	Glass transition temperature	K
T_{g_eq}	Glass transition temperature for melt with equilibrium c_{H2O}	K
T_{g_res}	Glass transition T for melt with maximum resorbed c_{H2O}	K
V_{H2Ol}	Volume of liquid H_2O in vesicles at room T	μm^3
V_{mH2O}	Molar volume of H_2O	$cm^3 \cdot mol^{-1}$
VND	Vesicle number density normalized to vesicle free sample volume	mm^{-3}
V_{ves}	Vesicle volume in the glass	μm^3
ΔP_{PS}	Difference between saturation P and P of phase separation	MPa
η	Melt viscosity	Pa·s
η_Tf	Viscosity at T_f, where vesicle shrinkage stops	Pa·s
ρ_{melt}	Melt density	$g \cdot cm^{-3}$
σ	Surface tension	$N \cdot m^{-1}$
τ_d	Decompression timescale	s
τ_{diff}	Diffusion timescale	s
Φ_{EOS}	Calculated porosity when shrinkage works until T_{g_eq}	%
Φ_{equ}	Equilibrium porosity	%
Φ_{glass}	Glass porosity	%
Φ_{RES}	Calculated porosity when shrinkage works until T_{g_res}	%

decompression was initiated. For the first pair of experiments, samples were decompressed from 200 MPa to P_{final} of 80 MPa and quenched by switching off the furnace, while the samples remained in the hot zone of the sample holder (normal quench = NQ). The sample CD49 underwent a non-isobaric NQ, with a monitored P drop of ~ 5–7 MPa during cooling of the argon pressure medium (NQ non-isobaric), while sample CD66 underwent an isobaric NQ ($\pm$ 0.1 MPa), with P being kept constant by pumping additional argon into the vessel. Sample CD74 (a replicate of CD50; Allabar et al. (2020), was decompressed to 70 MPa and quenched with MQ. An additional pair of experiments, samples CD37 and CD41, were decompressed to 80 and 90 MPa, respectively, then cooled with an unknown rate that must have been either non-isobaric NQ or MQ, because of a missing T decrease that would have indicated the capsule drop from the hot zone into the cool part of the sample holder. After re-weighing to exclude capsule leakage, the quenched samples, except of CD74, were cut along their cylinder axis. One half of each sample was prepared for SEM image analysis and the other halves were prepared to obtain double-sided polished thin sections with 89–210 µm thickness for Fourier Transform Infrared (FTIR) and transmitted light microscopy analysis. Thin section thickness was measured with a Mitutoyo digital micrometer ($\pm$ 3 µm). Sample CD74 was unwrapped from the capsule material and scanned using XCT.

Table 2 Summary of experimental conditions, results, and calculations

Sample	c_{H2Oini} [wt%]	T_d [K]	P_{final} [MPa]	dP/dt [MPa·s^{-1}]	q [K·s^{-1}]	$\log VND$ [mm^{-3}]	Φ_{glass} [%]	c_{H2OIR} [wt%]	c_{H2Oequ} [wt%]	τ_{diff}/τ_d	Φ_{equ} [%]	Φ_{EOS} [%]	Φ_{RES} [%]	T_f [K]	c_{H2Ores_TT} [wt%]	References
CD66	5.29±0.11	1323	80	0.17	16 isob	5.22	0.5±0.2	5.00±0.11	3.12	$5.7\cdot10^{-3}$	26.9	8.7	0.0	683	5.23	this study
CD49	5.28±0.09	1323	80	0.17	16 non isob	4.70	3.1±0.3	n.d	3.12	$8.8\cdot10^{-3}$	26.9	8.7	0.0	767	4.74	this study
CD41	5.29±0.09	1323	90	0.17	(44)*	5.22	1.1±0.2	5.23±0.05	3.34	$6.8\cdot10^{-3}$	22.7	--	--	753	5.11	this study
CD37	5.32±0.09	1323	80	0.17	(16 non isob.)*	5.17	1.9±0.2	5.08±0.06	3.12	$4.9\cdot10^{-3}$	27.2	--	--	725	4.97	this study
CD74 (XCT)	5.33±0.11	1323	70	0.17	44	n.d.	n.d.	n.d.	2.88	n.d.	32.3	12.1	1.9	810[+]	4.22	this study
~5.3 wt%																
CD40	5.17±0.09	1323	100	0.17	44	5.15	0.1±0.1	n.d.	3.56	$1.9\cdot10^{-2}$	17.9	5.8	0.0	784	5.21	AN18
CD42	5.20±0.09	1323	90	0.17	44	4.98	1.1±0.1	5.22±0.06	3.34	$9.8\cdot10^{-3}$	21.9	7.3	0.0	768	5.03	AA20a
CD63	5.30±0.10	1323	80	0.17	44	5.24	7.0±0.7	5.10±0.03	3.12	$2.9\cdot10^{-3}$	27.1	9.4	0.1	870	4.26	AN18
CD39	4.97±0.13	1323	80	0.17	44	5.17	4.5±0.5	5.00±0.05	3.12	$3.8\cdot10^{-3}$	24.0	8.1	0.0	859	4.31	AN18
CD91	5.33±0.10	1323	80	0.17	44	5.41	9.0±1.1	n.d.	3.12	$2.0\cdot10^{-3}$	27.3	9.5	0.2	910	4.11	AA20a
CD83	5.46±0.07	1323	80	0.17	44	5.78	3.2±1.0	n.d.	3.12	$1.6\cdot10^{-3}$	28.5	10.0	0.6	745	4.86	AA20a
CD50	5.30±0.09	1323	70	0.17	44	4.83	13.1±1.4	5.18±0.04	2.88	$3.4\cdot10^{-3}$	32.1	11.9	1.8	916	3.80	AN18
CD73	5.46±0.17	1323	60	0.17	44	5.41	18.5±2.2	n.d.	2.63	$8.9\cdot10^{-4}$	39.3	17.4	4.9	885	3.60	AA20a
CD92	5.10±0.09	1323	80	0.064	44	5.35	4.6±0.6	n.d.	3.12	$1.1\cdot10^{-3}$	25.2	8.6	0.0	839	4.39	AN18
CD78	5.12±0.05	1323	82	1.7	44	5.32	3.3±0.6	5.14±0.08	3.16	$3.5\cdot10^{-2}$	24.5	8.2	0.0	810	4.59	AN18
CD28	5.29±0.06	1323	95	1.7	44	5.05	0.5±0.1	5.25±0.04	3.45	$1.3\cdot10^{-1}$	20.8	6.8	0.0	755	5.24	AA20a
CD59	5.21±0.05	1373	110	1.7	44	5.48	0.1±0.1	n.d.	3.61	$2.2\cdot10^{-1}$	17.1	5.6	0.0	835	5.19	AA20a
CD55	5.22±0.05	1373	100	1.7	44	4.60	0.5±0.1	5.18±0.02	3.40	$3.9\cdot10^{-1}$	20.5	6.7	0.0	791	5.17	AA20a
CD57	5.32±0.07	1373	100	1.7	44	4.78	0.1±0.1	5.32±0.02	3.40	$3.5\cdot10^{-1}$	21.4	7.0	0.0	757	5.36	AA20a
CD51	5.27±0.11	1373	75	1.7	44	4.98	4.2±0.9	5.36±0.07	2.85	$5.1\cdot10^{-2}$	31.5	11.5	0.7	776	4.54	AN18
CD52	5.21±0.07	1373	90	0.17	44	4.96	1.6±0.4	5.32±0.02	3.19	$1.0\cdot10^{-2}$	24.2	8.0	0.0	784	4.94	AA20a
CD53	5.17±0.06	1373	80	0.17	44	4.95	1.5±0.2	5.21±0.03	2.96	$7.6\cdot10^{-3}$	28.2	9.6	0.0	733	4.92	AN18
~4.3 wt%																
CD87	4.31±0.10	1323	60	0.17	44	5.51	5.4±1.3	4.53±0.17	2.63	$8.0\cdot10^{-3}$	27.8	11.1	0.0	852	3.72	AA20a
CD85	4.30±0.13	1323	40	0.17	44	5.45	24.4±2.2	3.91±0.12	2.07	$1.8\cdot10^{-3}$	43.7	26.0	11.4	945	2.71	AA20a
~3.3 wt%																
CD94	3.43±0.05	1323	40	0.17	44	5.96	0.3±0.1	n.d.	2.07	$1.0\cdot10^{-2}$	32.2	17.6	1.6	748	3.36	AA20a
CD95	3.36±0.12	1323	20	0.17	44	6.37	15.4±2.1	n.d.	1.37	$1.1\cdot10^{-3}$	58.5	45.4	35.2	646	2.65	AA20a

All decompression experiments were hydrated at 200 MPa prior to decompression. Symbol definitions are given in Table 1

*Quench rate of these samples was unknown after the experiment, but a possible quench rate was derived from Φ_{glass} (for details see text). Therefore, Φ_{EOS} and Φ_{RES} were not calculated for these samples; isob. = isobaric quench; non isob. = non isobaric quench with a P drop

[†]T_f determined by XCT method

References: AN18: Allabar and Nowak (2018); AA20a: Allabar et al. (2020)

Quantification of cooling rate

For the IHPV with rapid quench setup, a cooling rate (q) of ~ 150 K·s^{-1} (RQ) was determined by Berndt et al. (2002) for dropping the capsule from the hot zone of the furnace into the cold part of the samples holder. The temperature at the bottom of the sample holder is 293–298 K at experimental T of up to 1523 K and 200 MPa (Berndt et al. 2002). However, for experiments from Allabar and Nowak (2018) and Allabar et al. (2020) the aim was to reduce tension crack formation in the samples during quench. Otherwise, samples will likely disintergrate and pieces may be lost during preparation. Thus, the experimental setup of the IHPV sample holder was modified by inserting a 35 mm brass cylinder at the bottom of the sample holder. This setup enables a medium quench rate (MQ) because the capsule stays slightly closer to the hot zone of the furnace during cooling, i.e., at $T > 298$ K. In order to quantify the quench rate of this setup, reference experiments where performed on two glass cylinders of the same geometry as for decompression experiment samples (5 mm diameter, 6.5 mm length) using haplogranite composition ($AOQ = Ab_{38}Or_{34}Qz_{28}$, Holtz et al. 1995; Nowak and Behrens 1995). The AOQ melts were hydrated with ~ 5.3 wt% H_2O in Au80Pd20 capsules at 200 MPa and 1523 K for 96 h. After hydration, one sample experienced the isobaric MQ protocol, while the other underwent an isobaric NQ. Doubly polished thin sections were prepared from the quenched glasses and the molecular H_2O and OH group absorption band intensities determined with FTIR (A_{5230} and A_{4520}, respectively). 20 and 23 measurements were performed on the NQ and RQ sample, respectively, with a spectral resolution of 4 cm^{-1} and 50 scans per measurement. A linear baseline subtraction (Behrens et al. 1996) and normalization to 1 mm sample thickness was applied. Cooling rates were then determined using the hydrous species geospeedometer (Zhang et al. 2000). For the MQ protocol, mean $A_{5230} = 0.793 \pm 0.08$ and $A_{4520} = 0.343 \pm 0.003$ yield a cooling rate of 44 ± 11 K·s^{-1}. For the NQ protocol, mean $A_{5230} = 0.769 \pm 0.002$ and $A_{4520} = 0.330 \pm 0.002$ give a cooling rate of 16 ± 3 K·s^{-1}. This NQ cooling rate is consistent with the logged T close to the sample during cooling, which showed nearly linear cooling from T_d down to ~ 573 K. The glass transition temperature (T_g) of this AOQ glass (at 5.3 wt% and a cooling rate of 16 K·s^{-1}) is at 660 K (Dingwell and Webb 1990; Giordano et al. 2008). Thus, linear cooling down to T_g can be assumed. The near sample T logs during NQ at P between 200 and 50 MPa show that the cooling rate is nearly independent of P in this range.

Determination of vesicle number density and glass porosity

Vesicle number density (VND) and Φ_{glass} were determined merely on the vesiculated central sample volume because this volume is of interest to study vesiculation driven by homogeneous phase separation. Heterogeneously nucleated fringe vesicles at the capsule wall and the drainage zone that is formed by diffusional loss of H_2O into fringe vesicles are experimental artifacts (e.g., Mangan and Sisson 2000; Iacono-Marziano et al. 2007; Preuss et al. 2016; Allabar and Nowak 2018; Allabar et al. 2020) and were therefore omitted for analysis.

Sample CD66 was analyzed with transmitted light microscopy on the thin section of the sample. Vesicles were counted during focusing through the sample and Φ_{glass} was determined using measured vesicles sizes. The VNDs in the other samples of this study were determined by analysis of the backscattered electron (BSE) images, because vesicles are large enough for a sufficiently high intersection probability. The BSE images were analyzed using ImageJ and the stereological 2–3D conversion using CSDCorrections (Higgins, 2000). The VND was normalized to vesicle free glass volume. An error in VND of ± 0.13 log units was estimated with an error propagation considering all steps that are prone to errors (Allabar et al. 2020). Errors of Φ_{glass} were provided by CSDCorrections in case of BSE image analysis. For transmitted light microscopy analysis, an error in Φ_{glass} was estimated with an error propagation calculation, using the error in sample thickness of ± 3 μm and assuming an error of 10% for vesicle size measurement and 5% for the vesicle count. A more detailed description of VND and Φ_{glass} analysis is given in Marxer et al. (2015) and Allabar et al. (2020).

FTIR micro-spectroscopy

Near-infrared measurements in transmission mode were carried out with a Hyperion 3000 IR-microscope connected to a Bruker Vertex v80 FTIR, using a CaF$_2$ beam splitter and an InSb single element detector together with a $15 \times$ Cassegrain objective. Samples of Allabar et al. (2020) and samples of this study were measured to determine the residual c_{H2O} in the glass between vesicles (c_{H2OIR}). Measurements were located between vesicles in the central sample volume or as close as possible to the vesicles at the margin of the central vesiculated volume (Fig. 1). The knife-edge aperture was adjusted for each measurement individually between 10×10 to 30×30 μm to ensure that the beam path was free of vesicles. This was checked by focusing through the entire sample volume in z direction at the measurement location. 50 scans were recorded per spectrum with a spectral resolution of
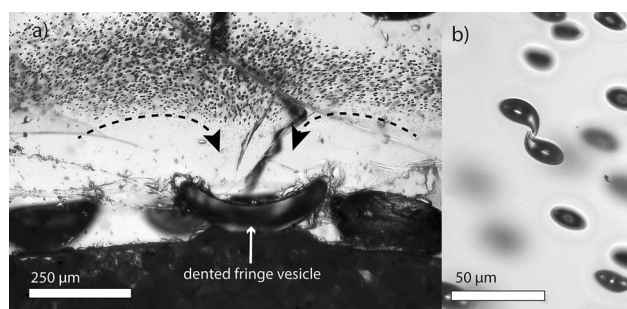
Fig. 1 **a** Transmitted light microscopy image of sample bottom of CD50 (Allabar and Nowak 2018). The fringe vesicles are dented and flow textures in the zone with small vesicles are visible. Large vesicles are surrounded by a vesicle free drainage zone. **b** Transmitted light microscopy image of vesicles within the central part of CD49. Vesicles positioned close to each other are often deformed and form a neck towards each other. Detailed capsule images are shown in the online resources of Allabar et al. (2020)

4 cm^{-1} using air as reference. At least five spots per sample were measured. For the determination of c_{H2OIR} from molecular H_2O (A_{5210}) and hydroxyl group absorbance (A_{4470}) the c_{H2O}-density relationship ($\rho[g \cdot cm^{-3}] = 2.47 - 0.013 \cdot c_{H2O}$ [wt%]) and linear molar extinction coefficients ($\varepsilon_{H2O} = 1.18$ and $\varepsilon_{OH} = 1.14$ l·mol^{-1} cm^{-1}) from Iacono-Marziano et al. (2007) were used.

To resolve c_{H2O} gradients with high spatial resolution between vesicles in the central vesiculated part of the sample CD73, mid-infrared measurements were performed using an attenuated total reflectance (ATR) objective (20x) mounted on the Hyperion3000 microscope in combination with a 64×64 focal plane array detector (FPA). The ATR germanium (Ge) crystal was brought in contact with the polished sample surface using a contact pressure of 3 (within a possible range of 1–5; ~4.4 N). At higher contact pressures the vesiculated glasses tend to break. A value of 3 is low enough to prevent cracking and is sufficient for reproducible peak heights of the fundamental OH stretching band at 3450 cm^{-1}. An Au-mirror was used as reference, spectral resolution was decreased to 16 cm^{-1} to minimize the noise associated with atmospheric water vapor (Lowenstern and Pitcher 2013) and 256 scans were accumulated for each spectrum. With these settings, 128×128 spectra were collected in 4 frames that cover a sample area of 70×70 µm. For each spectrum the peak height of the fundamental OH stretching band at 3450 cm^{-1} was determined after linear baseline subtraction anchored at 3760 and 2430 cm^{-1}. Calibration for absolute c_{H2O} for this method was not performed because the contact pressure, i.e., the energy of the light reaching the detector across the area of a frame, was not homogeneous. This is probably due to a tiny tilt of the Ge-ATR-crystal relative to the sample surface.

Raman micro-spectroscopy

Raman micro-spectroscopy (RMS) mapping was performed on sample CD73 at the same location as the FTIR mapping to quantify $c_{H2Oglass}$ gradients. A Renishaw InVia confocal Raman micro-spectrometer was used, equipped with a 532 nm ("green") laser, a 1800 grooves·mm^{-1} grating, and a Peltier-cooled CCD-detector. Laser power was set to 10%, corresponding to ~2.5 mW on the sample, which is low enough to avoid oxidation or dehydration of the samples (Di Genova et al. 2017). A 50× objective with a numerical aperture of 0.75 was used together with the high confocality setting to optimize for spatial resolution. The laser was focused at the sample surface, and it was checked whether the laser remained focused while moving across the mapped area. An area of 38×52 µm was mapped with one spectrum collected each µm (= 1976 spectra) from 100–4000 cm^{-1} with an acquisition time of 10 s. Laser intensity was checked before and after the mapping to confirm its stability. To obtain total H_2O concentration from the Raman spectra, a calibration was performed with hydrated reference samples from Marxer et al. (2015) (REF02-06 and one unpublished sample) with known c_{H2O} (1.37–5.60 wt%) from FTIR spectrsocopy. Two calibrations were used (e.g., Schiavi et al 2018): (1) calibration of the high wavenumber 3450 cm^{-1} band (HW) and (2) calibration of the ratio of the HW band and the low wavenumber (LW, 200–1250 cm^{-1}) aluminosilicate bands. A detailed description of calibration is given in the online resource "RMS and FTIR supplementary information".

XCT-measurements

The MQ sample (CD74) was scanned using a Zeiss Xradia 410 laboratory scanner system operating at 130 kV, a current of 76 µA, and the Xradia HE3 filter to reduce beam hardening effects. 2001 projections were collected with an exposure time of 10 s and the data were reconstructed using the Xradia proprietary algorithm to give a data volume with voxels of 2.06 µm edge length.

The image data were segmented and visualized using AVIZO© (ThermoFisher). After first defining a sample mask (manual refinement of a magic wand segmentation interpolated between every 100th slice to ensure capture of all edge contacting vesicles with thin films), the image data were segmented into glass and vesicle using the magic wand tool built into the Avizo segmentation workroom. Image noise and the smallest vesicle population were then removed by opening (kernel = 3) and closing (kernel = 3) and a 2D (perpendicular to sample axis) fill operation. Segmentation of the vesicle-gas and vesicle-liquid phases is challenging because of the small difference in greyscale value, and the

low signal–noise ratio in the raw data. However, after applying a 3D non-local means filter (5, 0.2, 10. 3) to the vesicles, segmentation could be achieved manually with a single click per vesicle. For comparison, two vesicles were segmented by manual assignment to the liquid and gas phase, before the volume of the different phases were calculated.

Results and discussion

In the samples of this study, we observed heterogeneously nucleated fringe vesicles attached to the capsule walls, a vesicle free drainage zone, and a finely vesiculated central volume formed by homogeneous phase separation as reported elsewhere (e.g., Iacono-Marziano et al. 2007; Allabar and Nowak 2018; Allabar et al. 2020). The logVND (in mm^{-3}) in the central sample volume ranges between 4.70 and 5.22 (analytical error $\pm$ 0.13 log units; Allabar et al. 2020), which is consistent with the log-VND observed in other samples with a c_{H2Oini} of $\sim$ 5.3 wt% (Table 2). Sample capsules after decompression and quench are often deformed with concave capsule walls. Furthermore, the fringe vesicles in all samples including those of Allabar et al. (2020) are strongly deformed with melt flow textures in their vicinity sometimes marked by small vesicles (Fig. 1a). The homogeneously distributed small vesicles in the sample center are spherical, except of few vesicle pairs where the inter vesicle wall is dimpled or a neck is formed from one vesicle to the other (Fig. 1b). Castro et al. (2012) explain such textures with the onset of coalescence, while McIntosh et al. (2014) attribute this to vesicle shrinkage during cooling.

Marxer et al. (2015) have also reported collapsed capsules with concave deformed walls after the decompression experiments (Figs. 6 and 15b, therein) and attribute this to vesicle shrinkage during cooling. Cooling causes a P drop within the capsule relative to quench pressure that drives capsule collapse during cooling. In contrast to this observation, an experimental setup capable to record the complete volume increase during decompression-induced degassing should freeze melt porosity (Φ_{melt}) at P_{final} during cooling. Consequently, capsules should show a convex shape. A concave deformation, however, as observed by Marxer et al. (2015) and in the experiments summarized in this study, can only be explained by a volume reduction of the capsule interior, i.e., shrinkage of H$_2$O vesicles, during cooling. Thus, we suggest that the textures observed at ambient conditions record vesicle shrinkage during cooling. These textures include the collapse of large fringe vesicles and flow textures preserved in the finely vesiculated glass in their vicinity. Strongly deformed vesicles attached to the capsule wall would not be able to

maintain a spherical shape if shrinkage were faster than the time required for the vesicle to adjust its geometry by reduction of surface energy. In the central sample volume, a low number of large vesicles ($\sim$ 200–300 μm diameter) that appear at low P_{final} (sample CD 73) preserve deformation (Allabar et al. 2020) while the small vesicles ($\sim$ 15 μm diameter) within the central sample volume are nearly spherical. The relaxation of deformed vesicles to a spherical shape depends on the radius (Toramaru, 1998):

$$t_{relax} = \frac{r \cdot \eta}{\sigma} \tag{1}$$

where r is radius in m, η is viscosity in Pa s and σ is surface tension in N m^{-1}. Thus, t_{relax} is more than 10 times larger for a vesicle 250 μm in diameter than for a vesicle with 15 μm diameter. However, a quantitative calculation is not possible here, because the quenched vesicle sizes do not represent the changing radii in the cooling melt, and in addition, η undergoes a complex evolution because of simultaneous cooling and melt rehydration.

Quantification of melt porosity prior to quench

The textural observations of the samples indicate vesicle shrinkage during cooling. Therefore, it is assumed that Φ_{glass} and c_{H2OIR} do not represent Φ_{melt} and c_{H2O} of the melt prior to cooling, respectively. Thus, Φ_{melt} and c_{H2O} at P_{final} and T_d are initially unknown. Nevertheless, the relative importance of H$_2$O diffusion during decompression can be determined, which is quantified by the ratio of diffusion timescale τ_{diff} to the timescale of decompression τ_d (Hajimirza et al. 2019). If the diffusion timescale is shorter than the decompression timescale ($\tau_{diff}/\tau_d \ll 1$), near-equilibrium degassing is facilitated and the melt porosity and c_{H2O} prior to quench can be calculated.

In the decompression experiments with hydrous phonolitic melt, the vesicles in the central melt volume form in a single event (Allabar and Nowak 2018; Allabar et al. 2020), so τ_d is the time between the P at which phase separation occurs and P_{final}. The τ_{diff} is defined as

$$\tau_{diff} \equiv \frac{l^2}{D_{H_2O}} \tag{2}$$

where D_{H2O} is the total H$_2$O diffusivity in mm^2 s^{-1} as a function of c_{H2O} in wt% and T in K, calculated after Fanara et al. (2013):

$$\log D_{H_2O} = -1.11 - 2.07 \log c_{H_2O} - \frac{(4827 - 4620 \log c_{H_2O})}{T} \tag{3}$$

The characteristic diffusion length l in mm is defined by the inter-vesicle distance calculated as follows (Hajimirza et al. 2019):

$$l = \frac{1 - \left(\frac{\Phi}{100}\right)^{\frac{1}{3}}}{\left(1 - \frac{\Phi}{100}\right)^{\frac{1}{3}}} \left(\frac{4\Phi}{3} \text{VND}\right)^{-\frac{1}{3}} \tag{4}$$

For a conservative estimate of l we use Φ_{glass} for calculations. A conservative estimate of D_{H2O}, and thus of τ_{diff}, is realized using the equilibrium c_{H2O} (c_{H2Oequ}) at the P_{final} of each experiment, which results in the slowest possible H_2O diffusivity. The c_{H2Oequ} at 1373 K for VAD79 phonolitic melt (Iacono-Marziano et al. 2007; Marxer et al. 2015) is calculated by:

$$c_{H_2O}^{1323K}[wt\%] = 0.2321 \cdot P[MPa]^{0.5928} \tag{5}$$

For the onset of vesiculation, we use 110, 70, and 50 MPa for samples with 5.3, 4.3, and 3.3 wt% c_{H2Oini}, respectively, to calculate τ_d. The given P's are 10 MPa above the respective P_{final}, at which vesicles are observed in the vitrified samples. It may be possible that vesiculation starts earlier at higher P and vesicles were completely resorbed in the high P_{final} experiments (see argumentation below). However, the usage the given P's constitutes a conservative estimate for τ_d. The obtained τ_{diff}/τ_d values are all $\ll 1$ (Table 2) suggesting near-equilibrium degassing during decompression prior to quench. The resulting equilibrium melt porosity at P_{final} (Φ_{equ}) prior to quench can be calculated (Gardner et al. 1999, Eq. 5 therein):

$$\Phi_{equ} = \left[\frac{\frac{\rho_{melt}}{M_{H_2O}} \cdot V_{mH2O} \cdot (c_{H_2Oini} - c_{H_2Oequ})}{1 + \left(\frac{\rho_{melt}}{M_{H_2O}} \cdot V_{mH2O} \cdot (c_{H_2Oini} - c_{H_2Oequ})\right)}\right] \tag{6}$$

where melt density ρ_{melt} (Ochs and Lange 1999) and molar volume of H_2O fluid V_{mH2O} (Duan and Zhang 2006) are calculated for equilibrium conditions at P_{final} prior to quench (Table 2). Furthermore, near-equilibrium degassing is evidenced by similar Φ_{glass} observed in the central volumes of samples decompressed with different dP/dt to a similar P_{final}. The samples with ~5.3 wt% c_{H2Oini} that are decompressed at T_d of 1323 K to 80–82 MPa reveal similar Φ_{glass} of 3.3–7.0% with no systematic dependence on dP/dt in the range between 0.064–1.7 MPa·s^{-1} (Allabar and Nowak 2018). If disequilibrium degassing occurred prior to quench,

significant increase in porosity with decreasing dP/dt at constant P_{final} would be expected, which is not observed here.

Since near-equilibrium degassing must have prevailed in the experiments, melt porosity equals Φ_{equ} and c_{H2O} of the melt equals c_{H2Oequ} prior to quench. This knowledge enables us to quantify vesicle shrinkage during cooling.

Vesicle shrinkage during cooling

For all samples, the Φ_{glass} observed at ambient conditions (0.1–24.4%) is significantly lower than the calculated Φ_{equ} prior to quench (17.1–58.5%, Table 2, Fig. 2). This is in line with c_{H2OIR} at ambient conditions (3.91–5.36 wt%) that are higher than c_{H2Oequ} prior to quench (1.37–3.61 wt%, Table 2). These discrepancies suggest that both significant vesicle shrinkage and H_2O resorption occurred in the experimentally decompressed samples during cooling.

The extent of vesicle shrinkage increases with lower q, as demonstrated by sample CD66 ($c_{H2Oini} = 5.22$ wt%; $P_{final} = 80$ MPa; $q = 16$ K·s^{-1} isobaric), which has a lower Φ_{glass} of 0.5% compared to MQ experiments with identical P_{final} and similar c_{H2Oini} ($q = 44$ K·s^{-1}; $\Phi_{glass} = 1.5$–9.0%). With slow cooling, more time is available for diffusion to resorb H_2O from the fluid back into the melt, and for the vesicle size to equilibrate to the decreasing internal vesicle P by viscous flow of the melt. The Φ_{glass} of 3.1% in CD 49 ($q = 16$ K·s^{-1} non-isobaric) is in the range of porosities of the MQ experiments. Vesicles of this sample shrunk less than expected for isobaric quench because the influence of decreasing P during cooling on V_{mH2O} and H_2O solubility in the melt dampens the effect of T decrease. When Φ_{glass} of the experiments CD41 and CD37 with unknown q are compared to the trend of experiments with 44 K·s^{-1} (Fig. 2), it can be estimated that CD41 ($P_{final} = 90$ MPa; $\Phi_{glass} = 1.1\%$) experienced a q of 44 K·s^{-1} and CD37 ($P_{final} = 80$ MPa; $\Phi_{glass} = 1.9\%$) a non-isobaric q with 16 K·s^{-1}.

Quantification of vesicle shrinkage during cooling

Vesicle shrinkage can be calculated when the conditions prior to quench are known. Note that resorption shrinkage requires c_{H2Oequ} being adjusted in the melt prior to cooling (Ryan et al. 2015). Otherwise, when the cooling-induced increase of H_2O solubility of the melt does not exceed H_2O supersaturation during cooling, no driving force for resorption of H_2O from the fluid phase back into the melt evolves. In our experiments both EOS- and H_2O resorption-shrinkage occurred because cooling started from Φ_{equ} and c_{H2Oequ}.

To demonstrate the contribution of each vesicle shrinkage mechanism to the overall shrinkage, we calculate in a first step solely EOS shrinkage down to T_g without any resorption (Marxer et al. 2015). For the melt with c_{H2Oequ} at the respective P_{final}, T_g was calculated ($= T_{g\_equ}$) using the
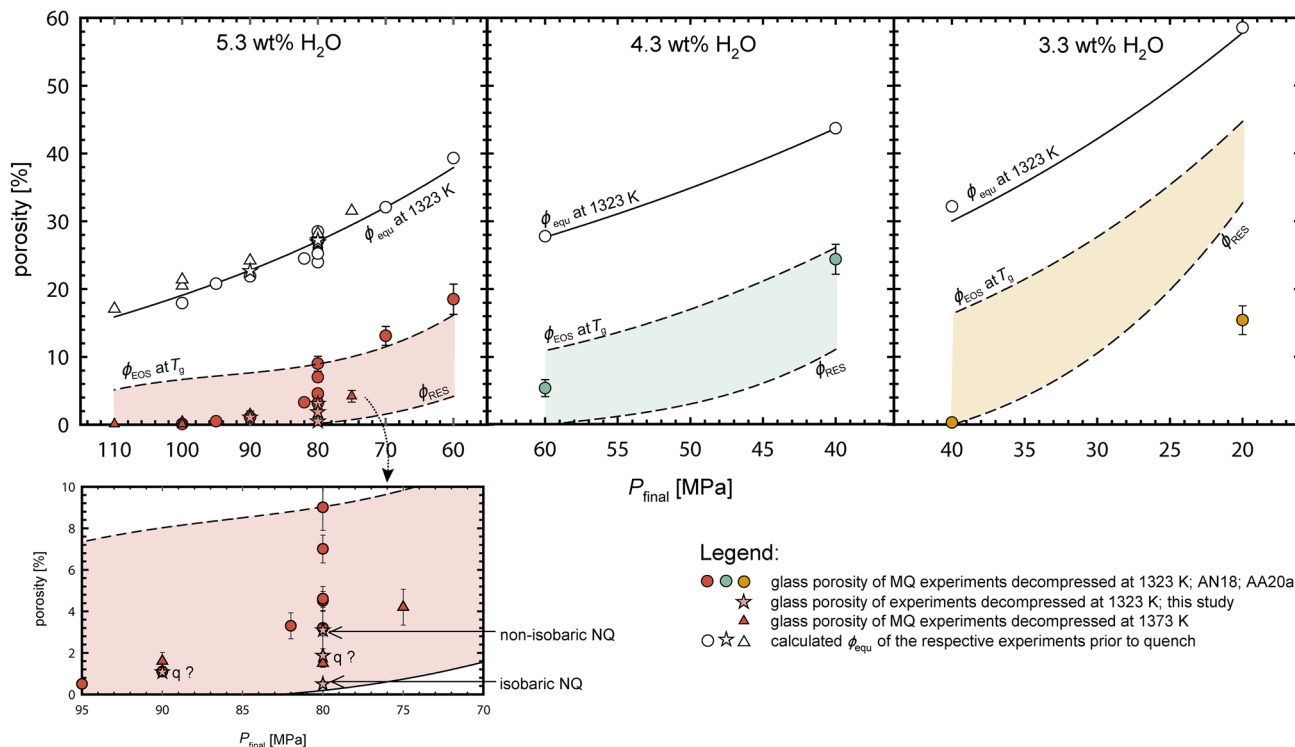
Fig. 2 Observed glass porosities (Φ_{glass}) vs. P_{final} for 5.3, 4.3 and 3.3 wt% c_{H2Oini}. Equilibrium porosity (Φ_{equ}, solid line) is calculated for 1323 K and 5.3, 4.3 and 3.3 wt% c_{H2Oini}, respectively. The deviation of individual equilibrium porosity from the Φ_{equ} curve originates from slight variation in initial H_2O concentration or a slightly increased decompression temperature of 1373 K (triangles). Φ_{EOS} represents the calculated porosity at T_g related to EOS-shrinkage.

Φ_{RES} is the minimum possible porosity taking additionally into account that H_2O is resorbed during cooling until T_{g_res} is reached, according to the H_2O solubility model of Shea (2017) (Eq. 8). Both Φ_{EOS} and Φ_{RES} are calculated for a cooling rate of 44 K s^{-1}. For details see text. The lower box is a zoomed excerpt of the 5.3 wt% c_{H2Oini} experiments for detailed visualization. References: AN18: Allabar and Nowak 2018; AA20a: Allabar et al. (2020)

viscosity model of Giordano et al. (2008) and the cooling rate (44 K·s^{-1}) dependent viscosity that defines the glass transition (log $\eta = 9.66$ Pa·s; Dingwell and Webb 1990) where vesicle shrinkage is assumed to stop. The V_{mH2O} at P_{final} and T_d or T_{g_equ} can then be calculated (EOS of H_2O, Duan and Zhang (2006) for $T > 673.15$ K; WaterSteamPro™ (Orlov et al. 1999-2020 Version 6.5.0.64) for $T < 673.15$ K). The ratio of $V_{mH2O}(P_{final}, T_{run})$ and $V_{mH2O}(P_{final}, T_{g\_equ})$ corresponds to the shrinkage factor B_s (Marxer et al. 2015). This factor is then used to calculate the glass porosity by Eq. 7 (Marxer et al. 2015, Eq. 4 therein) at T_g (Φ_{EOS}, Fig. 2) when shrinkage started from Φ_{equ}:

$$\Phi_{EOS} = \frac{\Phi_{equ}}{\Phi_{equ} - B_s \cdot (\Phi_{equ} - 100)} \cdot 100 \qquad (7)$$

However, this calculated Φ_{EOS} at T_g likely underestimates the real value, because the vesicles will effectively stop shrinking at a temperature $> T_g$ due to limited viscous flow with increasing melt viscosity.

In a second step, we additionally account for resorption shrinkage because sample porosity is further reduced

by H_2O resorption during cooling. Therefore, combined shrinkage by EOS and H_2O resorption was calculated using the rehydration quench method of Ryan et al. (2015) (Fig. 3). Here, it is considered that T_g continuously decreases during cooling due to the H_2O resorption of melt (i.e., viscosity reduction). Ultimately, the melt is quenched to a glass when the T_g curve and retrograde H_2O solubility curve intersect ($= T_{g\_res}$; Fig. 3) defining the residual c_{H2O} in the glass after maximum possible resorption (c_{H2Ores}). Here, the T-dependent solubility equation for phonolite from Shea et al. (2017) (which reproduces c_{H2Oequ} at 1323 K from Eq. 5 with $< 3\%$ relative deviation) was used to calculate temperature dependent solubility c_{H_2O} curves during isobaric cooling (Fig. 3):

$$c_{H_2O} = \frac{330P^{0.5} + 16P - 1.6P^{1.5}}{T} + 0.001\ P^{1.5} \qquad (8)$$

where P is in MPa and T in K. The T_g curve was calculated for a cooling rate of 44 K·s^{-1} (Giordano et al. 2008;
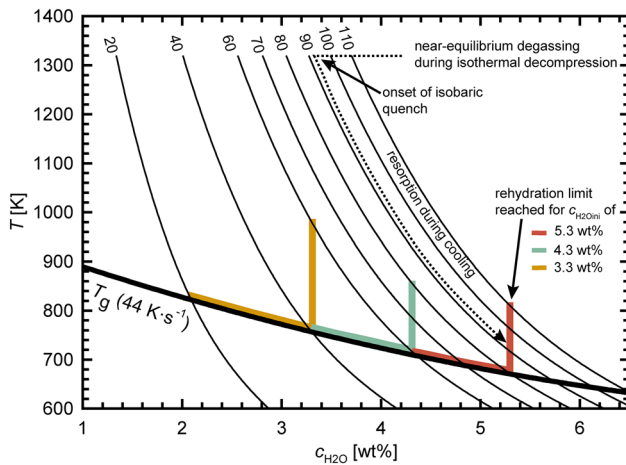
Fig. 3 Rehydration quench scenarios using the method of Ryan et al. (2015) for P_{final} of the decompression experiments with c_{H2Oini} of 5.3–3.3 wt%, summarized in Table 2. Isobaric H_2O solubility curves (thin black lines) for different P (in MPa) are calculated, using the H_2O-solubility equation for phonolitic melt from Shea et al. (2017) (Eq. 8). The T_g curve (thick black line) as a function of c_{H2O} for $q = 44$ K·s^{-1} was calculated with the viscosity model of Giordano et al. (2008) accounting for quench rate dependence of T_g (Dingwell and Webb 1990). The colored lines indicate the rehydration limit for the experiments summarized in Table 2 defined by maximum possible resorbed c_{H2O}. These lines follow the T_g curve as long as the maximum resorbed c_{H2O} is $< c_{H2Oini}$. When the cooling-induced solubility increase reaches c_{H2Oini} (vertical colored lines), rehydration can be completed, and all vesicles will be fully resorbed if diffusion time is sufficient

Dingwell and Webb 1990). Each cooling path is defined by the solubility curve, assuming that resorption effectively occurs until T_{g_res}. When the solubility reaches the c_{H2Oini} of the sample, T_{g_res} is equal to T_g of the melt with c_{H2Oini}. In this case, the degassed H_2O can be fully resorbed when the melt attains equilibrium H_2O content during cooling.

The possibility of complete resorption has consequences for experiments where the pressure difference required for (heterogeneous or homogeneous) phase separation (ΔP_{PS}) is intended to be determined. ΔP_{PS} is usually determined by finding the P at which vesicles are observable for the first time after decompression. If quench rates are used that allow vesicle shrinkage, vesicles may be fully resorbed until a certain pressure is reached and as a result ΔP_{PS} can be significantly overestimated by post mortem analysis of the vesiculated glasses. However, in this case, independent ΔP_{PS} estimates might be useful, e.g., using the widths of the drainage zone in quenched samples to calculate the time needed to develop the diffusion width of the zone were no vesicles were formed due to insufficient supersaturation (Allabar and Nowak 2018) or by performing in-situ decompression experiments (Masotta and Keppler 2017). In turn, for all samples quenched at P

for which the solubility curves in Fig. 3 cross the T_g curve instead of ending at the rehydration limit, it can be ensured that vesicles will be observable in these samples. Shrinkage and resorption could also decrease the *VND* observed in vitrified samples when small vesicles are resorbed while large vesicles are not resorbed completely. However, in the experiments studied here, vesicles are similarly sized and we do not observe an increase of *VND* with decreasing P_{final}, suggesting that either all vesicles are resorbed to sizes below optical resolution or all vesicles remain at sizes above optical resolution during cooling.

With T_{g_res} and the respective c_{H2Ores} the maximum extent of shrinkage and thus the minimum possible glass porosity (Φ_{RES}) was calculated (Fig. 2). Φ_{EOS} and Φ_{RES} define an area (Fig. 2), in which the glass porosity of the quenched experimental products are likely to be found, when they experienced equilibrium degassing prior to quench. At low P_{final}, one reason why this area becomes narrower is that the slopes of isobaric solubility curves are higher (Fig. 3), which results in less resorption.

Comparison of calculated with observed porosities

Within error, the Φ_{glass} of the experimental samples with $c_{H2O ini}$ of ~ 5.3 and ~ 4.3 wt% plot between the calculated Φ_{EOS} and Φ_{RES} (Fig. 2). At high P_{final}, the glass porosities follow the resorption trend and then approximate the EOS trend at low P_{final} and higher porosities. This can be attributed to the higher residual c_{H2O} in the melt at high P_{final} resulting in a faster H_2O diffusivity (Eq. 3) e.g., by half an order of magnitude at 100 MPa as compared to 60 MPa, assuming equilibrium H_2O content. Thus, resorption is expected to be more efficient at higher P_{final}. The variation of Φ_{glass} of the experiments quenched at a P_{final} of 80 MPa can be explained by slight variations in c_{H2Oini}, as it can also be seen in the variation of Φ_{equ} for the individual experimental samples as compared to the calculated Φ_{equ} as function of P_{final} for a sample with c_{H2Oini} of 5.3 wt% (Fig. 2).

The Φ_{glass} of sample CD94 with c_{H2Oini} of 3.3 wt% and P_{final} of 40 MPa is close to the calculated Φ_{RES} trend, which can be explained by the high log*VND* of 5.96. This value is almost one order of magnitude higher than the log*VND* of ~ 5 in the 5.3 wt% c_{H2Oini} experiments (Table 2). Despite the slower H_2O diffusivity, the inter-vesicle distance (< 10 μm) in the 3.3 wt% experiments is roughly half of that of the 5.3 wt% experiments, which in turn improves efficiency of H_2O resorption. This results in similarly low τ_{diff}/τ_d for experiments with c_{H2Oini} of 3.3 wt% as compared to experiments with higher c_{H2Oini} of 5.3 wt%. The glass porosity of CD95 with c_{H2Oini} of 3.3 wt% H_2O and a P_{final} of 20 MPa is below the minimum possible value (Φ_{RES}). Possibly, in this sample equilibrium porosity was not achieved prior to quench. An H_2O supersaturation prior to quench would counteract

resorption until the solubility curve exceeds the residual c_{H2O} of the melt. Vesicle shrinkage would then start from a melt with porosity $< \Phi_{equ}$, but solely by EOS-shrinkage. However, according to the calculations above, diffusion must have been fast enough for equilibrium degassing and viscous retardation of vesicle growth is not expected due to a low viscosity of 10^3–10^4 Pa s (Thomas et al. 1994). However, according to Toramaru (1998) the effective viscosity of a vesicle-rich silicate melt is larger for pure melt with identical c_{H2O} if the fluid phase is stored in a large *VND* of small isolated vesicles. The two experiments with 3.3 wt% c_{H2Oini} are those with the highest log*VND* of ~ 6. This high *VND* might have caused a high bulk viscosity, limiting equilibrium growth of the vesicles. Furthermore, the sample decompressed to 20 MPa might have an unpredictably low glass porosity, because it was quenched close to the critical point of H_2O, where slight changes in *T* and *P* have a large effect on fluid density and calculations close to this point might be prone to large errors. Therefore, these two experiments might not be suitable for the shrinkage calculations presented here, where degassing close to equilibrium prior to quench is a pre-requisite. Thus, the experiments with c_{H2Oini} of 3.3 wt% were not considered for the following calculations.

## Determination of T_f where vesicle shrinkage effectively stops

We conclude, that EOS and resorption driven vesicle shrinkage effectively stops at temperatures $T_f > T_{g\_res}$. This is based on the observation that Φ_{glass} of the investigated samples with 5.3 and 4.3 wt% c_{H2Oini} are higher than Φ_{RES} (Fig. 2). Different methods can be applied to determine T_f:

Determination of T_f via glass porosity

For the determination of T_f from Φ_{glass}, we assume that the observed glass porosity represents the equilibrium porosity of the supercooled melt at T_f, where vesicle shrinkage effectively stops. Equation 7 can be used to calculate the *T* dependent Φ_{equ}, and therefore, we find the temperature T_f (and the resulting ρ_{melt}, V_{mH2O} and H_2O solubility) at known P_{final} and c_{H2Oini}, where Φ_{glass} matches the calculated porosity (Fig. 4). The T_f for samples with 5.3 and 4.3 wt% c_{H2Oini} and a *q* of 44 K·s^{-1} range between 733 and 945 K, while T_f is lower at 16 K·s^{-1} with 683 and 767 K (Table 2).

Determination of T_f via the H_2O liquid to vesicle volume ratio—application of XCT analysis

An independent method for determining the extent of vesicle shrinkage is provided by the ratio of liquid H_2O volume
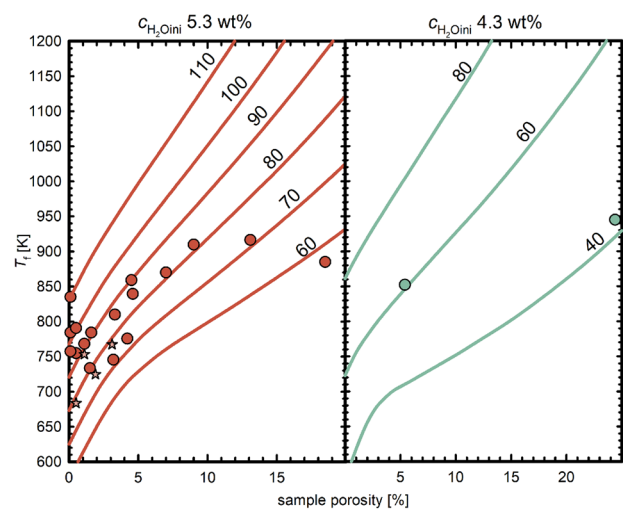

Fig. 4 Determination of T_f from glass porosity. Temperature dependent equilibrium porosities are exemplarily calculated for 5.3 and 4.3 wt% c_{H2Oini} at the different P_{final} (given in MPa next to each line) at which the samples were quenched. T_f was calculated based on the glass porosity, P_{final} and the individual c_{H2O} of each sample. The data points show the T_f that is derived from glass porosity of each sample. They do not all plot exactly on the curves calculated for the respective P_{final} due to small deviation of c_{H2Oini} of the experiments from the H_2O concentration that the curves were calculated for. Experiments with c_{H2Oini} of 3.3 wt% were not considered here because they may not have achieved equilibrium H_2O content prior to quench, which however is a pre-requisite for the T_f calculation (for details see text)

(V_{H2Ol}) in quenched vesicles to total vesicle volume (V_{ves}) using XCT analysis (McIntosh et al. 2015).

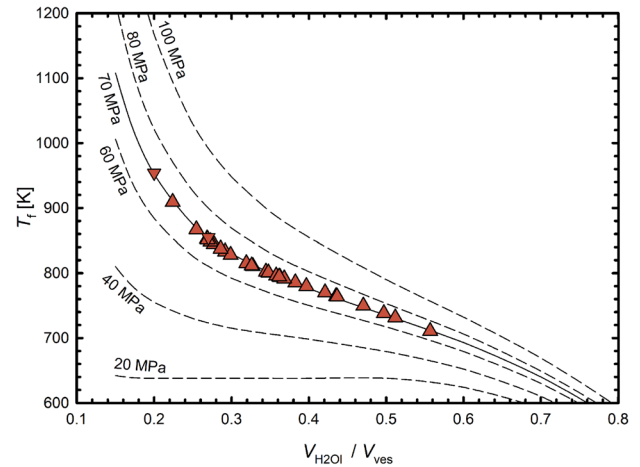During decompression, the exsolved H_2O fluid is supercritical because P_{final} and *T* exceed the critical point of H_2O. During cooling, vesicles shrink until T_f is reached. Below T_f the vesicle volume remains constant during further isochoric cooling and consequently, the pressure inside the vesicles starts to drop. The supercritical fluid follows a path of constant density until the liquid–vapor phase boundary is reached, after which the liquid–vapor ratio changes with the *P* in the vesicles following the water-steam equilibrium curve until ambient *T* is reached. H_2O present as vapor and liquid at room temperature results in an internal vesicle *P* of 0.035 bar. The volume of liquid water (water vapor can be neglected in this case due to its low density) gives an approximation of the amount of H_2O fluid trapped at T_f. As the amount of liquid water observed at ambient *T* would completely fill the vesicle volume at P_{final} as a single phase fluid, we can calculate T_f from the equation of state of H_2O. This method does not require knowledge of EOS- and H_2O resorption-contribution to shrinkage.

XCT-imaging reveals, that larger deformed vesicles are distributed within the central finely vesiculated volume of the MQ sample CD74 (Fig. 5a). The large vesicles may be ascended fringe vesicles or a product of coalescence (Allabar
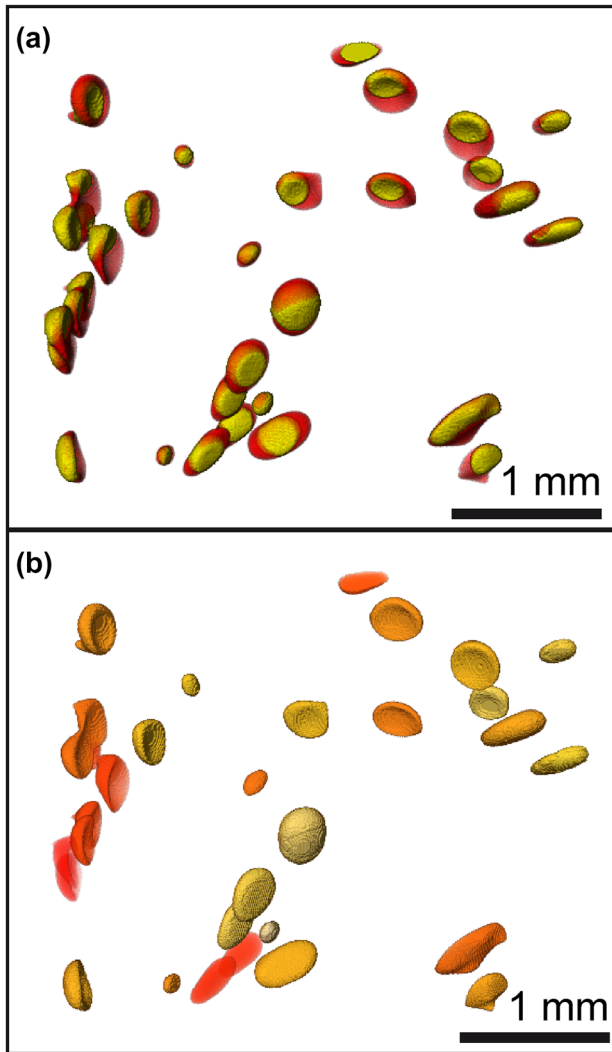
Fig. 5 **a** XCT-images of large vesicles in the central vesiculated volume of CD74 that are filled with vapor (yellow) and liquid H_2O (red) at ambient conditions. Volume of liquid H_2O to vesicle volume ratios were used to calculate T_f where vesicle shrinkage stops. Due to capillary forces, the liquid water is not gravitationally located at the bottom of each vesicle. **b** same vesicles color coded for T_f, with light yellow for high T_f towards orange for low T_f. Edge length of the XCT images are approximately 3.6 mm

Fig. 6 T_f's determined from individual large vesicles in CD74 using the ratio of the volume of liquid H_2O in the vesicle to the total vesicle volume based on XCT data (Fig. 5) handled by automated analysis (triangles up) and manual analysis (triangles down). The determined volume ratios at P_{final} of 70 MPa define a T_f range between 710 and 954 K for CD74. The additional dashed curves are exemplarily shown for different P_{final}
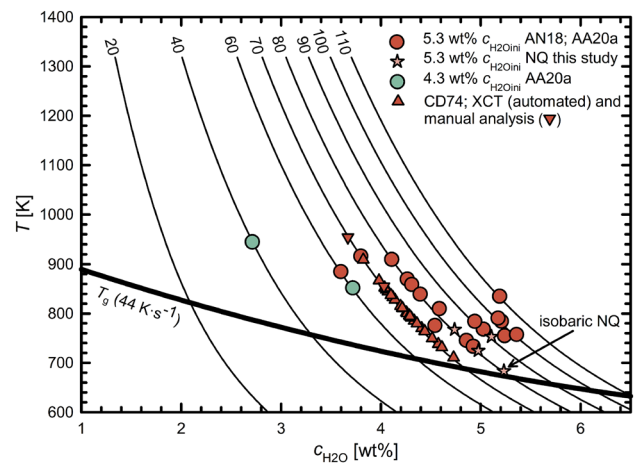
Fig. 7 Summarized T_f's of samples calculated from both Φ_{glass} (Fig. 4) and XCT data (Fig. 6) in the same plot as Fig. 3. Each solubility curve (black lines) is labeled with the corresponding P in MPa. T_f's are up to 200 K higher than T_g which means that vesicle shrinkage stops significantly before T_g is reached. Isobaric NQ (16 K·s^{-1}) reveals the lowest T_f because more time was available for vesicle shrinkage driven by H_2O resorption and viscous flow of the melt compared to MQ (44 K·s^{-1}). The XCT data based T_f's are qualitatively consistent with T_f's calculated from glass porosity. References: AN18: Allabar and Nowak (2018); AA20a: Allabar et al. (2020)

et al. 2020). The smaller dispersed spherical vesicles are close to the limit of XCT resolution and were therefore not included in the V_{H2Ol} analysis. Analysis of vesicles in CD74 yield V_{H2Ol} to V_{ves} ratios between 0.56 and 0.20, corresponding to T_f between 710 and 954 K, respectively (Fig. 6) with a random spatial distribution of T_f within the sample (Fig. 5b). The T_f estimates from XCT analysis are within the range of T_f derived from the glass porosity calculations (Fig. 7). The mean value of 810 K can be assumed, if cooling was homogeneous throughout the sample implying that a single temperature T_f is valid for the vesiculated part of the sample. However, we propose that vesicle shrinkage within an

experimental sample may be a complex process including competition of vesicles in close vicinity (including the small, finely dispersed vesicle population) and the ability of a vesicle to achieve efficient volume reduction by deformation that

will depend on its surrounding. These processes may lead to differences in T_f of individual vesicles.

Together, the methods of estimating T_f (Fig. 7) show that for samples with 5.3 and 4.3 wt% c_{H2Oini}, vesicle shrinkage stops up to 200 K above T_g, and that the relationship between T_f and P_{final} is similar to the relationship between T_g and P_{final}. We assume that T_f derived from Φ_{glass} reveals a mean T_f for the whole central sample volume comparable to the mean T_f from XCT analysis. Using T_f and the P_{final} for each sample, the theoretical residual c_{H2O} in the supercooled melt at T_f ($= c_{H2Ores\_Tf}$) can be calculated (Fig. 7), and used to define the viscosity at which vesicle shrinkage stops. The viscosity $\eta_{\_Tf}$ ranges from 10^6 to 10^8 Pa·s at 44 K·s^{-1} and appears to be independent of P_{final}. For cooling with 16 K·s^{-1}, we find a $\eta_{\_Tf}$ of 10^8 and 10^9 Pa·s due to lower T_f as a result of slower cooling.

At lower viscosities (above T_f) it is likely that the vesicles instantaneously shrink to their equilibrium size. This instantaneous growth and shrinkage has been shown in in-situ experiments (Masotta and Keppler 2014) demonstrating pressure cycling induced vesicle volume changes in a melt with a viscosity of 8.5·10^5 Pa·s.

Uncertainties of vesicle shrinkage calculations

The H_2O-solubility equation (Eq. 8) used here is based on experimentally determined H_2O solubility in phonolitic melt over P and T ranges between 20–395 MPa and 1123–1473 K (Shea 2017, Eq. 8 therein). Since there is no experimental access to low T and P H_2O-solubility data in phonolitic melt between liquidus T and T_g due to crystallization, the applicability of this solubility model is uncertain, but remains up to now the only option to estimate H_2O resorption. While it is assumed that towards lower T, phonolitic melts would exhibit a strong increase in H_2O solubility as seen in haplogranitic melt (Shea 2017; Liu et al. 2005), this remains unconstrained.

An alternative H_2O-solubility model, which is based on the assumption of thermodynamic equilibrium (Ottonello et al. 2018), allows further tests. However, it predicts a smaller increase of solubility with decreasing T, which contrasts with the high c_{H2OIR} measured in the glass between the vesicles (e.g., c_{H2Ores} of ~ 4.3 wt% calculated with the model for $P_{final} = 80$ MPa at T_{g_res}, compared to ~ 5.3 wt% derived from Eq. 8 and ~ 5 wt% measured in the glasses). H_2O resorption in samples of this study occurs in a T ranging between T_d and a temperature below the liquidus in the metastable state. In the H_2O-solubility model of Liu et al. (2005) for rhyolitic melts, experimental data determined below the liquidus are included, which cannot be described by thermodynamic equilibrium. Since the H_2O-solubility (Eq. 8) is based on these data, it is suggested that this dependence is

more suitable for quantifying resorption processes of supercooled melt apart from equilibrium.

A further uncertainty in our calculations is that pure H_2O is assumed to be in the vesicles rather than an H_2O fluid with dissolved silicate components, which may influence the EOS parameters. However, at such low P, the solubility of melt components in H_2O fluid is low (e.g., Stalder et al. 2000). Therefore, this will have only a minor influence on our calculations.

## H_2O concentrations measured by FTIR and Raman micro-spectroscopy

The results of the FTIR-ATR mapping and RMS mapping on sample CD73 are shown in Fig. 8. In both the FTIR-ATR-map and the RMS-map an increase in $c_{H2Oglass}$ towards vesicles is detected, testifying H_2O resorption during cooling. With both methods, this can be clearly seen in the case of the vesicle just below the glass surface (marked with an arrow in Fig. 8a), with a resorption halo intersecting the sample surface. However, the results of the two methods differ with respect to the area of increased $c_{H2Oglass}$ above this vesicle that appears to be larger in the RMS-map. Additionally, the resorption halos with increased $c_{H2Oglass}$ around intersected vesicles are clearly visible only in the FTIR-ATR-map. We attribute this to the different beam penetration depth of the two methods. In case of the FTIR-ATR measurements, the effective penetration depth is ~ 0.25 µm (calculation after Compton and Compton (1993) given in the online resource "RMS and FTIR supplementary information"). Penetration depth of the RMS measurement must be higher to explain the RMS data. To get an estimate on RMS-penetration depth, we used a VAD79 thin section that was polished to ~ 20 µm thickness and measured it on top of a Si single-crystal standard that is usually used for the performance check of the spectrometer. With the same measurement conditions as for the mapping of the vesiculated samples, we find a distinct Si-Raman signal although the laser beam was focused at the glass sample surface. Thus, the penetration depth of the laser is > 20 µm. However, the effective penetration depth that quantitatively determines the c_{H2O} result is unknown. The large laser penetration depth is consistent with the study of Everall (2000), who finds that depth resolution of Raman spectroscopy is limited and usually worse than expected. Depth resolution gets worse by focusing into the sample volume, such that a 5 µm focus depth results in an illuminated depth of ~ 18 µm at a refractive index of 1.5 (Everall 2000). For glasses with homogeneously dissolved H_2O, it is usually suggested to use an optimal focus depth where HW and LW bands are at a maximum intensity (~ 5–10 µm focus depth depending on glass composition; Schiavi et al. 2018; Di Genova et al.

Fig. 8 **a** Transmitted light microscopy image of the mapped area of ▶ CD73 focused at the sample surface. The arrow is pointing at the central intact vesicle that is located ~1 μm below the surface, as indicated by the light diffraction rings. The frames indicate the areas of FTIR-ATR and Raman micro-spectroscopy (RMS)-mapping. **b** FTIR-ATR map based on 128×128 MIR spectra representing a sample area of 70×70 μm stitched by 4 frames (64×64 spectra each) showing a slight lateral offset. Spectra of each 64×64 frame were monitored simultaneously with a focal plane array MIR detector. Quantitative c_{H2O} determination was not calibrated due to a small tilt of the Ge-ATR crystal relative to the sample surface. Therefore, the pixel are color coded for the peak height of the 3450 cm^{-1} fundamental OH stretching band, representing total dissolved H_2O near the surface of the intersected sample. **c** RMS-map: color coded c_{H2O} concentrations derived from Rama spectra. RMS measurements that are affected by epoxy or carbon relicts (mostly within the intersected vesicles from preparation and previous carbon coating for SEM imaging), are colored black


(a) transmitted light microscopy image of the sample surface

(b) FTIR-ATR-map

(c) RMS-map
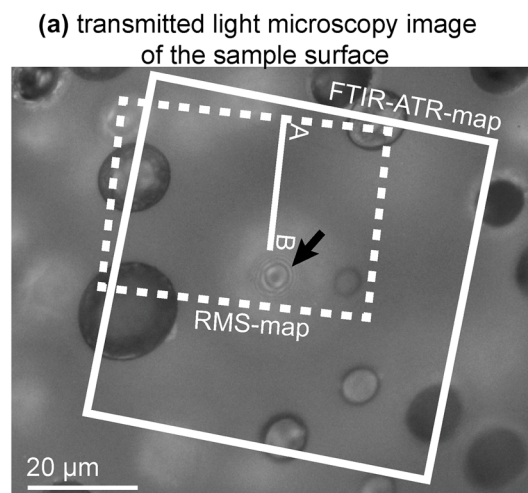
2017) because this reduces the error in c_{H2O} by focus inaccuracies. However, this approach should not be used for samples inhomogeneous in c_{H2O} for which a high spatial resolution *and* depth resolution is desired.

The large penetration depth using RMS of at least 20 μm has to be considered for the interpretation of $c_{H2Oglass}$ between vesicles. In detail, a c_{H2O} profile extracted from the RMS-map between two vesicles below the surface is shown by the A-B profile (Figs. 8a, c, 9). In transmitted light, a diameter of ~20 μm of the vesicles below the surface of the A-B profile was determined. The vesicle at the profile end B is ~1 μm below the surface, which is also indicated by the diffraction rings on the transmitted light microscopy image of the sample surface (Fig. 8a). The other vesicle at B is slightly deeper (Fig. 9). In the A-B profile (Fig. 9) the c_{H2O} determined from the HW calibration (3450 cm^{-1} band only, i.e., total H_2O) decreases when approaching vesicles that are several microns below the surface, while the c_{H2O} from HW/LW calibration further increases. The latter is related to the HW/LW calibration that reflects H_2O concentration per glass volume and is thus independent from the measured glass volume. A lower c_{H2O} near the vesicle at the profile end A is measured because the vesicle is located deeper below the sample surface. Compared to the vesicle at profile end B, which is closer to the surface (Fig. 9), a larger glass volume with less H_2O is measured at profile end A. This dilutes the Raman signal of resorption halos near the vesicle (Fig. 9). The same dilution problem occurs when measuring in the vicinity of intersected vesicles. Because of the large penetration depth of Raman spectroscopy measurements, the increased $c_{H2Oglass}$ around the vesicle, which extends only a few micrometers away from the vesicle, is diluted by H_2O poorer glass underneath (Fig. A3 in online resource "RMS and FTIR supplementary information"). Thus, resorption halos of intersected vesicles are clearly visible only in the FTIR-ATR-map.
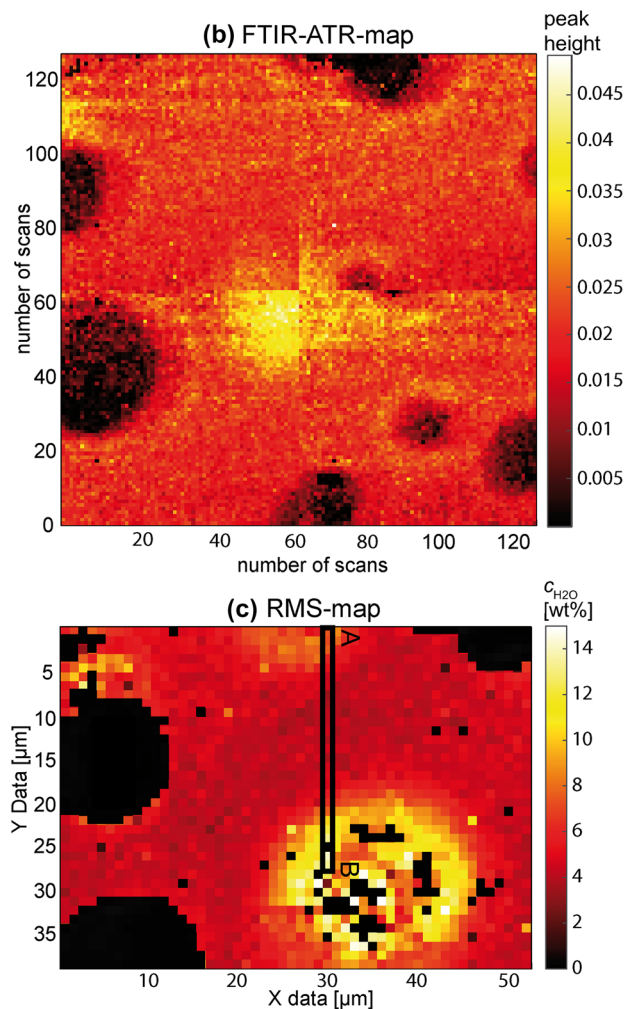
Despite the high penetration depth, we can use the H_2O contents from the RMS-map, which are not influenced by a vesicle in the measured volume. Theoretically, the HW/LW values with vesicles in the probed volume represent the H_2O content in the glass above the vesicle. However, we do not know whether the vesicle wall has a reflectance effect
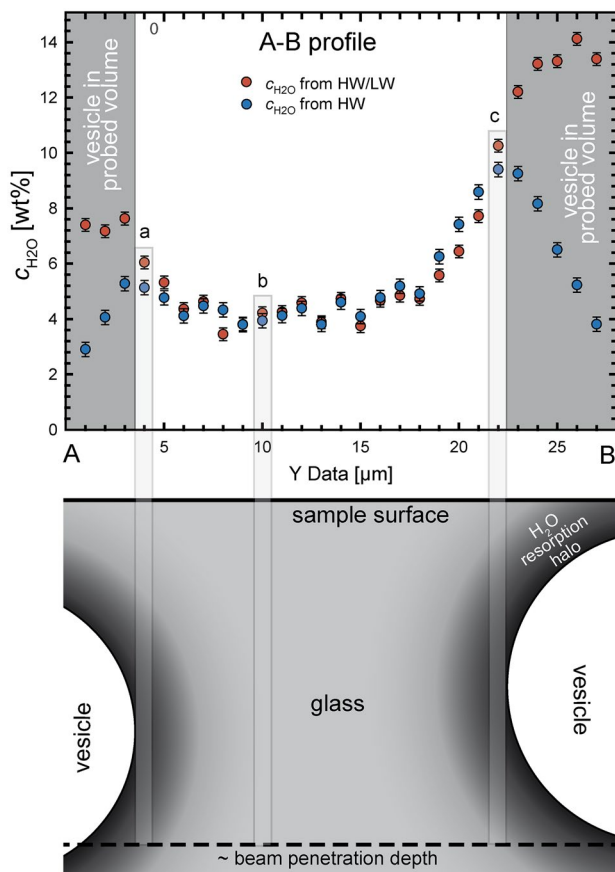
Fig. 9 Raman measured c_{H2O}—distance profile from position A to B as indicated in Fig. 8a, c. c_{H2O} from both HW and HW/LW calibration, is shown. Errors in c_{H2O} relate to the errors of calibration using hydrous VAD79 samples with different c_{H2O} (for details see online resource "RMS and FTIR supplementary information"). Below is a schematic illustration of the AB intersection of the sample below the surface. The vesicle at profile end A is positioned slightly deeper than the vesicle at the end B, which is ~ 1 μm below the surface. In the schematic intersection, the vesicle is drawn slightly deeper because the profile approaches the vesicle slightly lateral. The penetration depth of the laser beam during RMS measurements was determined to be at least 20 μm as indicated by the dashed line. Thus, the measurements with a vesicle in the probed beam yield different c_{H2O} values, dependent on HW and HW/LW calibration (data in grey areas; for details see text). All other measurements are unaffected by the vesicles. The highlighted bars indicate the illuminated volume yielding the resulting c_{H2O} to which they are connected in the plot above. The c_{H2O} at position a is lower than at position c because the high c_{H2O} of the H_2O resorption halo (shaded in black to dark grey) around the vesicle A is more diluted by H_2O poorer glass towards the sample surface compared to vesicle B

on the laser beam, which could distort the signal. Because of this uncertainty, we only consider measurements without vesicles in the probed volume. This is the case for measurements for which the HW and HW/LW calibration provide identical results within error (Fig. 9). We exclude all measurements from further interpretation, where the deviation of

the two values is greater than the relative change to the nearest value (Fig. 9, data with grey background). In the sample volume between the vesicles, a relatively homogeneous c_{H2O} of ~ 4.3 wt% is measured, which is significantly higher than calculated equilibrium c_{H2O} of 2.6 wt% at P_{final}. McIntosh et al. (2014) found ~ 20 μm diffusion profiles (with 12 μm half fall distance) in a phonolitic sample after rapid cooling within 3–10 s at 100 MPa. Therefore, it can be assumed that sample CD73 with diffusion lengths of ~ 10 μm and cooling within ~ 20 s has adjusted to the measured $c_{H2Oglass}$ of 4.3 wt% between the vesicles by resorption, although the melt had a low equilibrium c_{H2O} of ~ 2.6 wt% at P_{final} prior to cooling. We attribute the steep increase of c_{H2O} towards the vesicles to resorption at a late stage, where solubility strongly increases and concurrently, diffusivity decreases during cooling, becoming too slow for equilibrating the entire supercooled melt volume between the vesicles. Thus, the shape of such diffusion profiles results from the interplay of the timescale of cooling with the H_2O solubility increase and diffusivity decrease.

All c_{H2O} values measured between the vesicles of CD73 are above the calculated c_{H2Ores_Tf}. This is also the case for the NIR-FTIR transmission measurements through the glass without vesicles in the beam (Table 2). These measurements resemble a mean c_{H2O} between vesicles, but with unknown contribution of steep H_2O gradients towards vesicles. Nevertheless, the general observation of higher c_{H2O} in the glass compared to calculated values may indicate, that further H_2O diffusion occurs below T_f without further vesicle shrinkage (McIntosh et al. 2014). Assuming isochoric behavior of vesicles below T_f, H_2O diffusion from fluid to melt or glass below T_f changes the proportions of H_2O liquid and vapor observed at ambient T and may affect the T_f determination using XCT data. To test this, the liquid H_2O proportion in small vesicles of the pervasive clouds need to be analyzed in the future, where resorption is expected to be much more effective due to short diffusion distance than in the large vesicles that were used here. Alternatively, the discrepancies between c_{H2Ores_Tf} and c_{H2O} measured in the glasses can also originate from an underestimation of H_2O solubility towards low T by Eq. 8. Additionally to the discussion of experiment CD95 above, this could be an alternative reason for the mismatch between calculated and observed porosity.

Impact of experimental technique on vesicle shrinkage

Quantification of vesicle shrinkage in post-mortem analyzed H_2O-vesicle bearing samples requires knowledge of the experimental apparatus and the quench technique used (Fig. 10). When samples are quenched isobarically, EOS-shrinkage and resorption will be driven by T drop only (case 1 in Fig. 10). For a non-isobaric quench, shrinkage
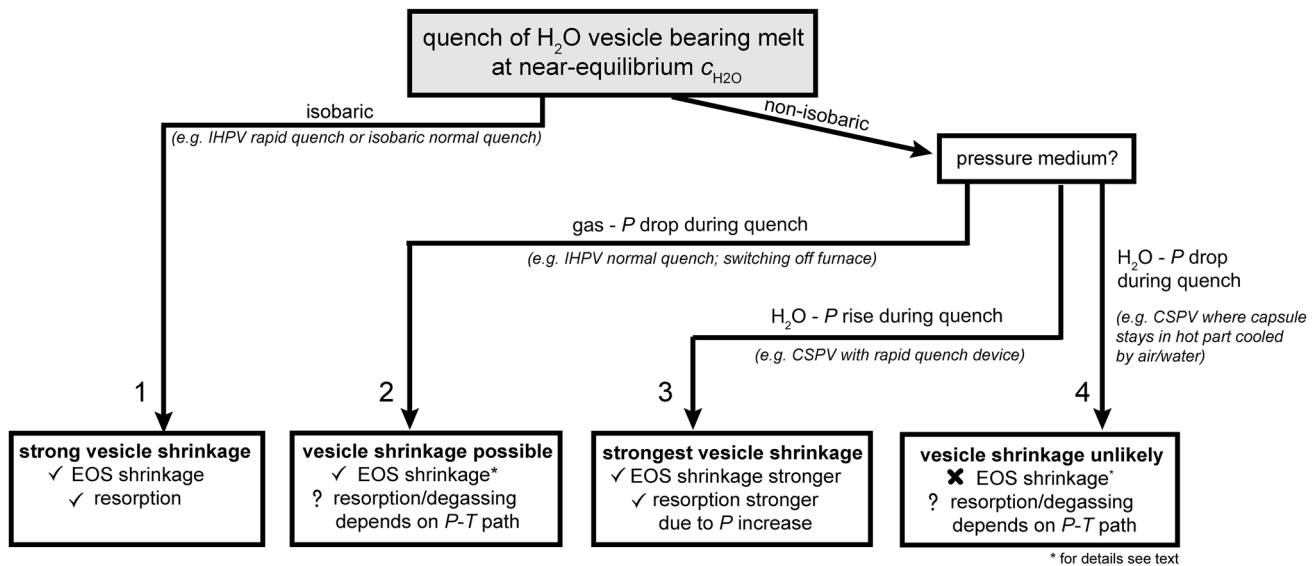
Fig. 10 Flowchart for illustrating the impact of different experimental quench techniques on H_2O-vesicle shrinkage in melts that reached near equilibrium c_{H2O} prior to quench. For a constant cooling rate, vesicle shrinkage and the single contributions (EOS- and resorption-shrinkage) will vary according to the shown quench conditions

will depend on the pressure medium that surrounds the sample and on the magnitude of pressure drop. When gas is used as pressure medium, P drops during cooling (CD49, this study). However, the P drop within the autoclave is less than that expected from a simple EOS calculation of the gas because only part of the gas volume of the IHPV is heated prior to quench. Nevertheless, V_{mH2O} decreases stronger during cooling than the V_{mgas} of the pressure medium. The pressure inside the vesicle will drop relative to the pressure medium and EOS shrinkage is facilitated (case 2). Test experiments in cold seal pressure vessels (CSPV), using H_2O as pressure medium, revealed that P may rise by up to 10 MPa during cooling when a rapid quench device is used because the hot capsule and parts of the guide rod heats the water in the cold part of the vessel by dropping in it. In this case, the strongest vesicle shrinkage is possible because the P increase supports resorption by solubility increase and compression of H_2O according to the EOS (case 3). If the sample remains in the hot section and the vessel is cooled by compressed air or water externally (e.g., Larsen and Gardner 2004), both the pressure inside the autoclave and the vesicles will drop during cooling according to EOS of H_2O, provided the P is not actively held constant. Because there is no P difference between the vesicles and the pressure medium, there will be no driving force for EOS-shrinkage (case 4). However, during cooling accompanied with a P drop, the retrograde T dependence of H_2O solubility will compete with the P-induced solubility decrease. Shrinkage in such an experiment is unlikely or will be of minor extent.

However, the prerequisite for shrinkage to occur at all is that some time for melt relaxation and diffusion is given. Theoretically, a sample has to cool infinitely fast to prevent vesicle shrinkage. The experiments summarized in this study belong to case 1 (MQ and NQ isobaric) and case 2 (CD49).

Review of experimentally derived porosities in phonolitic melt

Numerous decompression experiments have been performed using hydrous phonolitic melts (Larsen and Gardner 2004; Iacono-Marziano et al. 2007; Larsen 2008; Mongrain et al. 2008; Shea et al. 2010; Gardner 2012; Marxer et al. 2015; Preuss et al. 2016; Allabar and Nowak 2018; Allabar et al. 2020). When these data are compiled with the data of this study (online resource "Literature review") we can evaluate the effect of vesicle shrinkage during cooling also in these experiments, which are quenched with more commonly used rapid quench protocols (> 100 K s^{-1}). We include only such data where H_2O was the only volatile, degassing occurred in a closed system and glass porosity and VND were reported for experiments quenched at $P_{final} > 22.1$ MPa (above the critical point of H_2O).

For the compiled experimental data, we calculated whether near equilibrium H_2O content can be adjusted prior to quench (see calculations described above). Therefore, when available, the solubility data of each study were used for H_2O solubility at given run conditions. Otherwise, the general H_2O-solubility dependence for phonolitic melt (Eq. 8) was used and H_2O diffusivity was calculated with
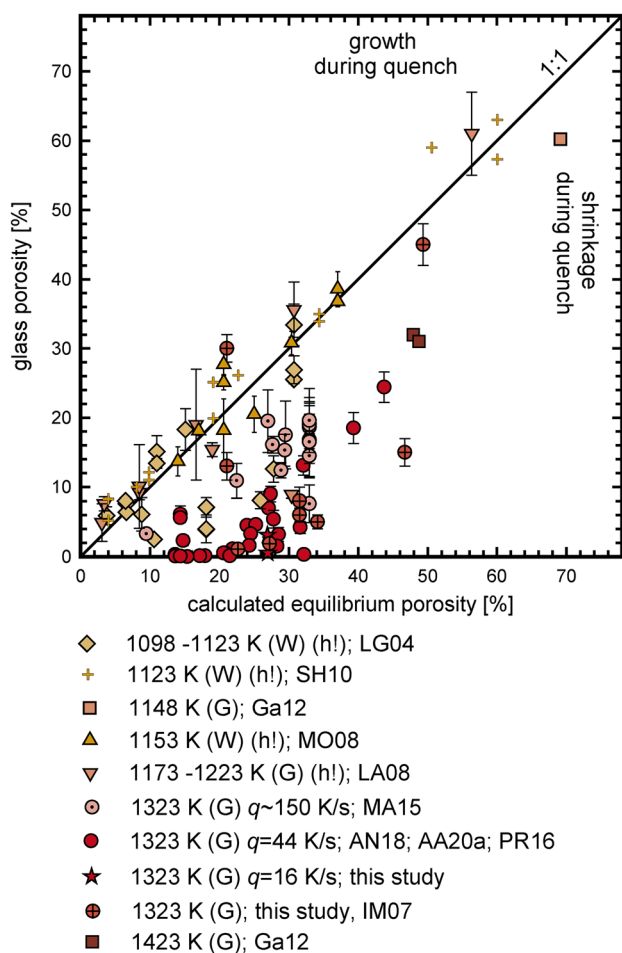
Fig. 11 Observed glass porosities vs. calculated equilibrium porosities for all decompression experiments with hydrous phonolitic melt composition, in which near-equilibrium degassing was facilitated prior to quench. (G) gas as pressure medium, (W) water as pressure medium. When q and error bars are not given, they are unknown. (h!) hydration vesicles might have been present prior to decompression due to the use of powder as starting material and H_2O supersaturated conditions prior to decompression. The experiments with melts containing hydration vesicles are the only ones plotting close to the 1:1 line, suggesting that no vesicle shrinkage occurred. The presence of a pre-existing fluid phase, however, can shift the glass porosities of the quenched samples to higher values towards or above the 1:1 line, although shrinkage occurred. Additionally, other reasons might also influence the glass porosity of these samples (see text). All data of other samples plot below the 1:1 line indicating vesicle shrinkage during cooling. A faster cooling rate (150 K·s^{-1}) leads to slightly less shrinkage (MA15) compared to slower cooling (44–16 K·s^{-1}; this study) References: LG04: Larsen and Gardner (2004); SH10: Shea et al. (2010); GA12: Gardner (2012); MO08: Mongrain et al. (2008); LA08: Larsen (2008); MA15: Marxer et al. (2015); AN18: Allabar and Nowak (2018); AA20a: Allabar et al. (2020); PR16: Preuss et al. (2016); IM07: Iacono-Marziano et al. (2007). Compilation of data can be found in the online resource "Literature Review"

Eq. 3 (Fanara et al. 2013). For all experiments, in which near-equilibrium porosity was adjusted prior to quench, the equilibrium porosity was calculated. The Φ_{glass} vs. Φ_{equ} is shown in Fig. 11 . In about half of the decompression experiments, vesicle shrinkage has likely occurred during cooling ($\Phi_{glass} < \Phi_{equ}$), despite faster quench rates (150–200 K s^{-1}) than in our study. The occurrence of vesicle shrinkage even at these high cooling rates is consistent with the large resorption-induced H_2O gradients towards vesicles rims found by McIntosh et al. (2014) in phonolitic glasses after cooling within 3–10 s from T_d to ambient T. The varying degrees of vesicle shrinkage presented in in Fig. 11 can be attributed to the following parameters:

Different experimental techniques

Experiments from studies using gas as pressure medium ((G) in Fig. 11) experienced a near isobaric quench (Case 1, Fig. 10), and showed large degrees of vesicle shrinkage, varying with quench rate (Fig. 11). For most studies using H_2O as pressure medium ((W) in Fig. 11) the actual quench rates and P changes during cooling are not known. Thus, direct comparison is not possible. One study reports a slight P increase of 5 MPa during quench (Case 3, Mongrain et al. 2008). Therefore, stronger vesicle shrinkage is expected but not observed (Fig. 11). This is likely due to higher cooling rate (> 100 K/s) compared to the studies using gas as pressure medium and the possibility of pre-existing hydration vesicles (see below).

Run temperature

Φ_{equ} increases with T_d and consequently the difference between the experimental T_d and T_f increases, enhancing vesicle shrinkage. The compiled data suggest an increase in vesicle shrinkage with increasing T_d. However, several mechanisms contribute to shrinkage, and run temperature is not solely responsible for the varying degree of vesicle shrinkage.

Hydration vesicles prior to decompression

For some experiments, glass powder was used as starting material. During hydration, H_2O vesicles can remain in the hydrated melt at H_2O supersaturated conditions prior to decompression, resulting in a melt with up to 12% porosity prior to decompression (Larsen 2008). These pre-existing fluid vesicles can cause artificially high glass porosities close to, or above the equilibrium line. Vesicle shrinkage might therefore still have occurred during cooling.

Crystallization

Some experiments (Mongrain et al. 2008; Larsen and Gardner 2004; Larsen 2008; Shea et al. 2010) were performed below the liquidus and crystals are reported or documented in the SEM images. Crystals increase the bulk viscosity (e.g., Costa 2005), which could decrease the degree of vesicle shrinkage due to the shift of T_f towards higher values.

Conclusion

Significant vesicle shrinkage can occur during cooling of vesicle-bearing silicate melts that achieved near-equilibrium c_{H2O} during decompression. The degree of vesicle shrinkage (EOS- and H_2O-resorption shrinkage) varies with experimental technique and quench style, with shrinkage enhanced by high residual c_{H2O} in the melt (i.e., P_{final}), increasing T_d, and slower quench rates.

The procedures presented here demonstrate how vesicle shrinkage can be determined, and how we can gain insight into the processes controlling shrinkage for experimentally vesiculated and quenched samples. While we can extract semi-quantitative information that constrains whether melt degassing is occurring in equilibrium or disequilibrium, we highlight the need for improved understanding of EOS- and resorption shrinkage through both in-situ decompression experiments and numerical modelling.

The present study was limited to phonolitic melts, but while the processes controlling shrinkage will be less pronounced in rhyolitic melts, they should still be important, and shrinkage will be especially significant for decompression experiments on melts with high H_2O diffusivity and low melt viscosity. It is therefore critical to consider vesicle shrinkage before porosity and c_{H2O} data from postmortem samples of decompression experiments are used for interpreting vesiculation of silicate melts. Otherwise, melt porosity is significantly underestimated leading to a false interpretation of the onset of coalescence, percolation or the distinction between equilibrium or dis-equilibrium degassing of a melt.

References

Allabar A, Nowak M (2018) Message in a bottle: spontaneous phase separation of hydrous Vesuvius melt even at low decompression rates. Earth Planet Sci Lett 501:192–201

Allabar A, Salis Gross E, Nowak M (2020) The effect of initial H_2O concentration on decompression-induced phase separation and degassing of hydrous phonolitic melt. Contrib Mineral Petrol. https://doi.org/10.1007/s00410-020-1659-2

Behrens H et al (1996) Near-infrared spectroscopic determination of water species in glasses of the system $MAlSi_3O_8$(M=Li, Na, K): an interlaboratory study. Chem Geol 128:41–63

Berndt J, Liebske C, Holtz F, Freise M, Nowak M, Ziegenbein D, Hurkuck W, Koepke J (2002) A combined rapid-quench and H_2-membrane setup for internally heated pressure vessels: description and application for water solubility in basaltic melts. Am Mineral 87:1717–1726

Castro JM, Burgisser A, Schipper CI, Mancini S (2012) Mechanisms of bubble coalescence in silicic magmas. Bull Volcanol 74:2339–2352

Compton SV, Compton DAC (1993) Optimization of data recorded by internal reflectance spectroscopy. In: Coleman PB (ed) Practical Sampling Techniques for Infrared Analysis. CRC Press, Boca Raton, Florida, pp 55–92

Costa A (2005) Viscosity of high crystal content melts: dependence on solid fraction. Geophys Res Lett 32:1–5

Di Genova D, Sicola S, Romano C, Vona A, Fanara S, Spina L (2017) Effect of iron and nanolites on Raman spectra of volcanic glasses: a reassessment of existing strategies to estimate the water content. Chem Geol 475:76–86

Dingwell DB, Webb SL (1990) Relaxation in silicate melts. Eur J Mineral 2:427–449

Duan ZH, Zhang ZG (2006) Equation of state of the H_2O, CO_2, and H_2O-CO_2 systems up to 10 GPa and 2573.15 K: molecular dynamics simulations with ab initio potential surface. Geochim Cosmochim Acta 70:2311–2324

Everall NJ (2000) Confocal Raman microscopy: why the depth resolution and spatial accuracy can be much worse than you think. Appl Spectrosc 54:1515–1520

Fanara S, Behrens H, Zhang YX (2013) Water diffusion in potassium-rich phonolitic and trachytic melts. Chem Geol 346:149–161

Gardner JE (2012) Surface tension and bubble nucleation in phonolite magmas. Geochim Cosmochim Acta 76:93–102

Gardner JE, Hilton M, Carroll MR (1999) Experimental constraints on degassing of magma: isothermal bubble growth during continuous decompression from high pressure. Earth Planet Sci Lett 168:201–218

Gardner JE, Wadsworth FB, Llewellin EW, Warkins JM, Coumans JP (2019) Experimental constraints on the textures and origin of obsidian pyroclasts. Bull Volcanol 81:22

Giachetti et al (2019) Bubble coalescence and percolation threshold in expanding rhyolitic magma. Geochem Geophys 20:1054–1074

Giordano D, Russell JK, Dingwell DB (2008) Viscosity of magmatic liquids: a model. Earth Planet Sci Lett 271:123–134

Gonnermann HM, Manga M (2007) The fluid mechanics inside a volcano. Annu Rev Fluid Mech 39:321–356

Hajimirza S, Gonnermann HM, Gardner JE, Giachetti T (2019) Predicting homogeneous bubble nucleation in rhyolite. JGR Solid Earth 124:2395–2416

Higgins MD (2000) Measurement of crystal size distributions. Am Mineral 85:1105–1116

Holtz F, Behrens H, Dingwell DB, Johannes W (1995) H$_2$O solubility in haplogranitic melts: compositional, pressure, and temperature dependence. Am Mineral 80:94–108

Iacono-Marziano G, Schmidt BC, Dolfi D (2007) Equilibrium and disequilibrium degassing of a phonolitic melt (Vesuvius AD 79 "white pumice") simulated by decompression experiments. J Volcanol Geotherm Res 161:151–164

Larsen JF (2008) Heterogeneous bubble nucleation and disequilibrium H2O exsolution in Vesuvius K-phonolite melts. J Volcanol Geotherm Res 175:278–288

Larsen JF, Gardner JE (2004) Experimental study of water degassing from phonolite melts: implications for volatile oversaturation during magmatic ascent. J Volcanol Geotherm Res 134:109–124

Lindoo A, Larsen JF, Cashman KV, Dunn AL, Neill OK (2016) An experimental study of permeability development as a function of crystal-free melt viscosity. Earth Planet Sci Lett 435:45–54

Liu Y, Zhang Y, Behrens H (2005) Solubility of H$_2$O in rhyolitic melts at low pressures and a new empirical model for mixed H$_2$O–CO$_2$ solubility in rhyolitic melts. J Volcanol Geotherm Res 143:219–235

Lowenstern JB, Pitcher BW (2013) Analysis of H$_2$O in silicate glass using attenuated total reflectance (ATR) micro-FTIR spectroscopy. Am Mineral 98:1660–1668

Mangan M, Sisson T (2000) Delayed, disequilibrium degassing in rhyolite magma: decompression experiments and implications for explosive volcanism. Earth Planet Sci Lett 183:441–455

Marxer H, Bellucci P, Nowak M (2015) Degassing of H$_2$O in a phonolitic melt: a closer look at decompression experiments. J Volcanol Geotherm Res 297:109–124

Masotta M, Keppler H (2017) A new hydrothermal moissanite cell apparatus for optical in-situ observations at high pressure and high temperature, with applications to bubble nucleation in silicate melts. Am Mineral 102:2022–2031

McIntosh I, Llewellin E, Humphreys M, Nichols A, Burgisser A, Schipper CI, Larsen J (2014) Distribution of dissolved water in magmatic glass records growth and resorption of bubbles. Earth Planet Sci Lett 401:1–11

McIntosh et al. (2015) 'Practical' glass transition temperatures of vesicular glasses: a combined FTIR-XRCT approach. Abstract, 10th Silicate melt workshop. La Petite Pierre, France

Mongrain J, Larsen JF, King PL (2008) Rapid water exsolution, degassing, and bubble collapse observed experimentally in K-phonolite melts. J Volcanol Geotherm Res 173:178–184

Nowak M, Behrens H (1995) The speciation of water in granitic glasses and melts determined by in situ near-infrared spectroscopy. Geochim Cosmochim Acta 59:3445–3450

Ochs FA, Lange AR (1999) The density of hydrous magmatic liquids. Science 283:1314–1317

Orlov KA, Alexandrov AA, Ochkov VF, Ochkov AV (1999–2020) WaterSteamPro™ Version 6.5.0.64. Moscow Power Engineering Institute (Technical University)

Ottonello G, Richet P, Papale P (2018) Bulk solubility and speciation of H$_2$O in silicate melts. Chem Geol 479:176–187

Preuss O, Marxer H, Ulmer S, Wolf J, Nowak M (2016) Degassing of hydrous trachytic Campi Flegrei and phonolitic Vesuvius melts: experimental limitations and chances to study homogeneous bubble nucleation. Am Mineral 101:859–875

Ryan AG, Russel JK, Nichols ARL, Hess KU, Porritt LA (2015) Experiments and models on H$_2$O retrograde solubility in volcanic systems. Am Mineral 100:774–786

Schiavi F, Bolfan-Casanova N, Withers AC, Médard E, Laumonier M, Laporte D, Flaherty T, Gómez-Ulla A (2018) Water quantification in silicate glasses by Raman spectroscopy: correcting for the effects of confocality, density and ferric iron. Chem Geol 483:312–331

Schmidt BC, Behrens H (2008) Water solubility in phonolite melts: influence of melt composition and temperature. Chem Geol 256:259–268

Shea T (2017) Bubble nucleation in magmas: a dominantly heterogeneous process? J Volcanol Geotherm Res 343:155–170

Shea T, Gurioli L, Larsen JF, Houghton BF, Hammer JE, Cashman KV (2010) Linking experimental and natural vesicle textures in Vesuvius 79AD white pumice. J Volcanol Geotherm Res 192:69–84

Sparks RSJ (1978) The dynamics of bubble formation and growth in magmas: a review and analysis. J Volcanol Geotherm Res 3:1–37

Spoor CF, Zonneveld FW, Macho GA (1993) Linear measurements of cortical bone and dental enamel by computed tomography: applications and problems. Am J Phys Anthropol 91:469–484

Stalder R, Ulmer P, Thompson AB, Günther D (2000) Experimental approach to constrain second critical end points in fluid/silicate systems: near-solidus fluids and melts in the system albite-H$_2$O. Am Mineral 85:68–77

Thomas N, Jaupart C, Vergniolle S (1994) On the vesicularity of pumice. J Volcanol Geotherm Res 99:633–715

Toramaru A (1998) Formation of propagation pattern in two-phase flow systems with application to volcanic eruptions. Geophys J 95:613–623

Zhang Y, Xu Z, Behrens H (2000) Hydrous species geospeedometer in rhyolite: Improved calibration and application. Geochim Cosmochim Acta 64:3347–3355